

Exotic properties and manipulation in 2D semimetal α - $\text{Mn}_2\text{B}_2(\text{OH})_2$: a theoretical study

Pingwei Liu,¹ Dan Liu,^{1,*} Shixin Song,¹ Kang Li,¹ Xueyong Yuan,^{1,2} and Jie Guan^{1,†}

¹*School of Physics, Southeast University, Nanjing, 211189, PRC*

²*Key Laboratory of Quantum Materials and Devices of Ministry of Education, Southeast University, Nanjing, 211189, PRC*

(Dated: December 10, 2024)

Most functional materials possess one single outstanding property and are limited to be used for a particular purpose. Instead of integrating materials with different functions into one module, designing materials with controllable multi-functions is more promising for the electronic industry. In this study, we investigate an unexplored α -phase of two-dimensional (2D) $\text{Mn}_2\text{B}_2(\text{OH})_2$ theoretically. Eighteen distinct electrical polarizations, characterized by three different magnitudes and twelve different directions, are found in this phase. The switch of the electrical polarizations is also linked to an observed splitting of band structures between different spin states and the ferroelasticity of the system. The manipulation of these properties can be realized through controlling the alignment of Mn-OH-Mn chains. Additionally, the approximately honeycomb lattice for the atomic layer of boron indicate the potential superconductivity in the system. The diverse and tunable properties make the proposed material as an outstanding candidate for sensing applications at the 2D limit.

I. INTRODUCTION

Since the successful isolation of graphene in 2004 [1], 2D materials have garnered considerable attention and efforts in both fundamental research and industry applications. Over the past decade, a myriad of 2D functional materials has been synthesised in experiment or predicted in theory, such as 2D ferroelectric materials [2–9], ferromagnetic materials [10–15], superconductors [16–20], etc. To broaden the application of 2D functional materials, efforts have been invested into integrating 2D materials with different functionalities within single system, such as heterostructures [13, 21–25]. Further exciting advances in this field include the realization of magnetoelectric multiferroics through the coupling between the magnetic polarization and the spin helix [26, 27] and the creation of intrinsic electric dipoles in 2D magnetic bilayers by a relative rotation [28, 29]. This direct method has achieved significant progress in artificial regulation of physical properties. However, the strict preparation conditions and the relatively weak coupling between the composed 2D materials make this method difficult to apply on a large scale. Thus, searching 2D materials with intrinsic and controllable multiple properties remains an exciting topic of research.

Here, *ab initio* calculations unveil diverse tunable ferroic properties in a previously unexplored α -phase of 2D material $\text{Mn}_2\text{B}_2(\text{OH})_2$ (*MBOH*). This material displays a ferroelectric (*FE*) behavior originating from the ordered arrangement of hydroxyl radicals bridging the neighboring Mn atoms. The formed Mn-OH-Mn (*MOM*) chains distribute on both sides of a flat monolayer of boron with a nearly-honeycomb lattice (*nh-B*). The electrical polarization of each individual side can

have six different orientations and the system exhibits eighteen distinct polarization states in total, which are manipulable by altering the direction of *MOM* chains. Within this polarization manipulating process, this 2D material shows a ferroelastic behavior, indicating a coupling between ferroelectricity and ferroelasticity. The α -phase *MBOH* exhibits a preference of antiferromagnetism, with magnetic moments of Mn atoms on different sides pointing in opposite directions. By independently controlling the *MOM* chains on each side of *nh-B*, the degeneracy of the electronic states in spin-up and spin-down channels can be regulated.

II. COMPUTATIONAL TECHNIQUES

Our calculations of the atomic structures, electrical and magnetic properties have been performed using DFT as implemented in the VASP [30, 31] code. We used the Perdew-Burke-Ernzerhof (PBE) [32] exchange-correlation functional. The DFT+U approximation is employed with $U=3$ eV and $J=1$ eV imposed on *3d* orbitals of Mn [33]. Periodic boundary conditions have been used throughout the study, with monolayers represented by a periodic array of slabs separated by a 20 Å thick vacuum region. The calculations were performed using the projector augmented wave (PAW) method [31] and 560 eV as energy cutoff. The reciprocal space has been sampled by a fine grid [34] of $12 \times 12 \times 1$ *k*-points in the 2D Brillouin zone (BZ). All geometries have been optimized using the conjugate gradient (CG) method [35], until none of the residual Hellmann-Feynman forces exceeded 10^{-2} eV/Å. The phonon spectrum was calculated using a $6 \times 6 \times 1$ supercell, and the real-space force constants of supercells were calculated using density-functional perturbation theory (DFPT) as implemented in VASP [36].

* liudan2@seu.edu.cn

† guanjie@seu.edu.cn

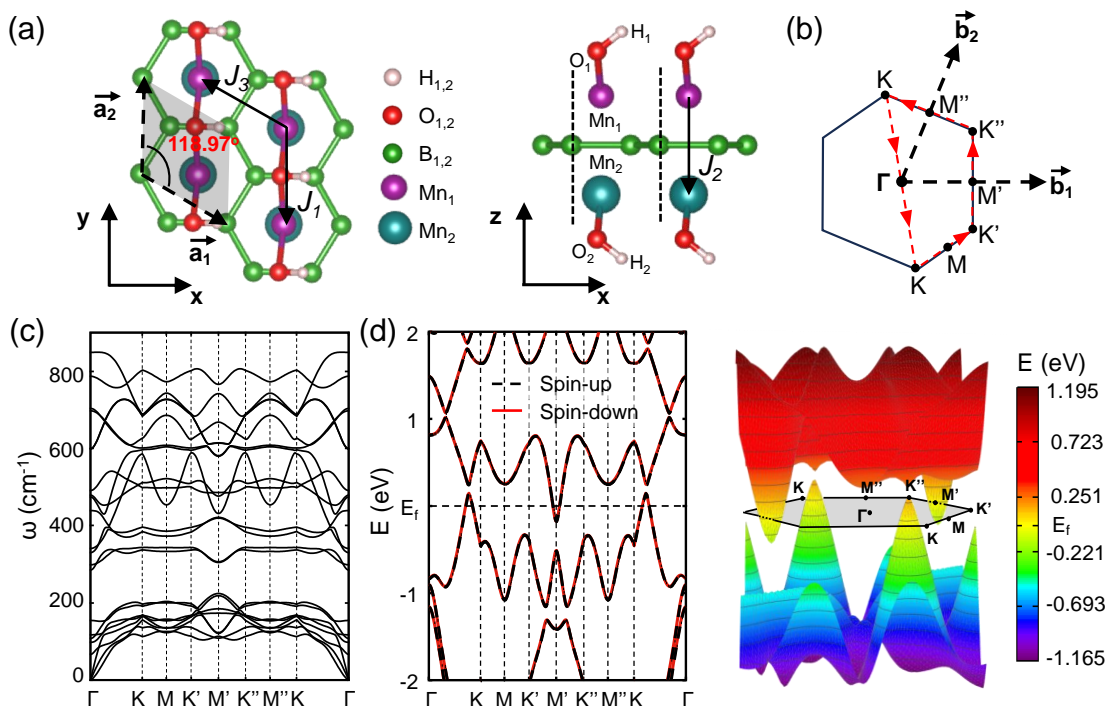


FIG. 1. (a) Atomic structure of 2D $\text{Mn}_2\text{B}_2(\text{OH})_2$. Mn atoms with different spins are presented in purple and green. The unit cell is highlighted by the transparent grey area which is a slightly distorted rhombus. The corresponding Brillouin zone and high symmetry points are exhibited in (b). DFT-PBE calculated phonon spectra is presented in (c). (d) Spin polarized electronic band structure and three-dimensional plot of the two bands below and above the fermi level.

III. RESULTS

A. Atomic structure, stability and electronic properties

Commencing with the precursor material MnB [37], our investigation explores various possible allotropes of MBOH with different magnetic orders and emphasize on the most stable one, named as α -phase, are shown in Fig. 1(a). **The strategy and details used to exploring the $-\text{OH}$ decorated MnB is presented in the Appendix A.** In α -phase MBOH , an atomic monolayer of boron with a nearly-honeycomb lattice is established. The adjacent Mn atoms, interconnected via hydroxyl radicals ($-\text{OH}$), are distributed on both sides of the boron layer. The unit cell contains two boron atoms, labelled as $B_{1,2}$, two Mn atoms, and two $-\text{OH}$ radicals. The subscripts 1 or 2 for Mn, O, H means whether an atom lies above (1) or below (2) the $nh-B$ as shown in the right panel of Fig. 1(a). The lattice of the α -phase is a slightly distorted hexagonal lattice, with lattice constants $a_1 = 3.14 \text{ \AA}$, $a_2 = 3.04 \text{ \AA}$, and an angle of 118.97° between \vec{a}_1 and \vec{a}_2 . Consequently, the first BZ is also a distorted hexagonal lattice, as shown in Fig. 1(b) with the distortion exaggerated. To validate the stability of the α -phase, we calculated the phonon spectrum and the results are shown in Fig. 1(c). No imaginary frequency is detected, which means α -phase is dynamically stable. **We have also**

confirmed the dynamic stability of the α -phase by performing canonical molecular dynamics (MD) simulation at room temperature of 300 K of 5 ps which are presented in Appendix C.

DFT-PBE calculations of electronic band structure are presented in Fig. 1(d). The results indicate that the α -phase MBOH is a semimetal, in which electron and hole pockets coexist on the Fermi surface. Analyzing the 2D band structure in Fig. 1(d), we observe that the valence band maxima (VBM) resides at the pathway from Γ to K , while conduction band minimum (CBM) is located at the M' . To ensure no crucial electronic information is overlooked in the 2D band structure, a three-dimensional band structure was also calculated to provide a comprehensive view of all details. The dispersion of the two bands above and below the Fermi surface across the entire k -space is exhibited in the right panel of Fig. 1(d). **In the most stable α -phase, an interesting antiferromagnetic (AFM) order called A-type AFM (A-AFM) is found with antiferromagnetically coupled ferromagnetic Mn layers.** The band structure exhibits a typical anti-ferromagnetic (AFM) behavior, where band dispersion for spin-up and spin-down states are degenerate. We also analysis the magnetic information by calculating the spin-polarized projected density of state, as presented in Fig. 9 of Appendix B. **It confirms that the magnetic moments are mainly contributed by the layer of Mn_1 and Mn_2 which point in opposite directions.**

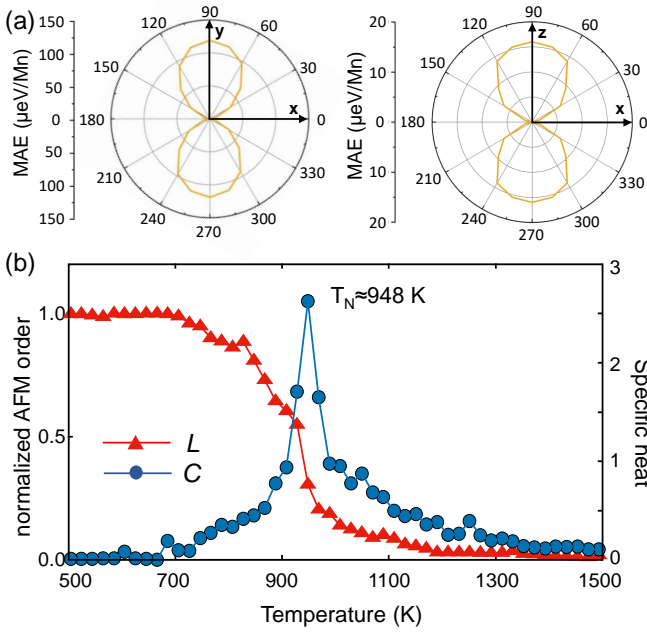


FIG. 2. (a) The DFT calculated MAE as a function of spin orientation. (b) MC simulated specific heat and normalized AFM order parameter L as a function of temperature. The AFM order parameter is defined as $L = S_u - S_l$, where S is the normalized spin and u/l denotes the upper and lower layers of Mn bilayers.

The magnetic anisotropy is also calculated by rotating the spin orientation. As shown in Fig. 2(a), the magnetic easy axis lies on the atomic plane and is along the x -axis. The magnetocrystalline anisotropy energy (MAE) is estimated to be around $120 \mu\text{eV}/\text{Mn}$ atom. As shown in Fig. 1(a), here we consider the nearest-neighbor exchange constant J_1 , next-nearest-neighbor exchange constant J_2 , and next-next-nearest-neighbor exchange constant J_3 to determine the magnetic order of the system. Based on the optimized structure of its ground state, through mapping the DFT energy to the Heisenberg model with normalized spins $|S| = 1$, these magnetic exchange coupling constants are derived to be 12.79 meV , -55.47 meV and 2.52 meV . Both J_1 and J_3 indicating a intralayer ferromagnetism, while J_2 prefers a interlayer antiferromagnetism of Mn_1 and Mn_2 atomic layers. Such a configuration of J is not frustrated, which co-stabilize the layered A-AFM order. Based on the above exchange coupling coefficients, the MC method was employed to simulate the magnetic transition. Its Neel temperature T_N is estimated to be 948 K , as indicated by the peak of specific heat shown in Fig. 2(b).

B. Ferroic properties and tunable electrical polarization

As seen in the atomic structure, the $-\text{OH}$ radicals are oriented in the direction perpendicular to the MOM

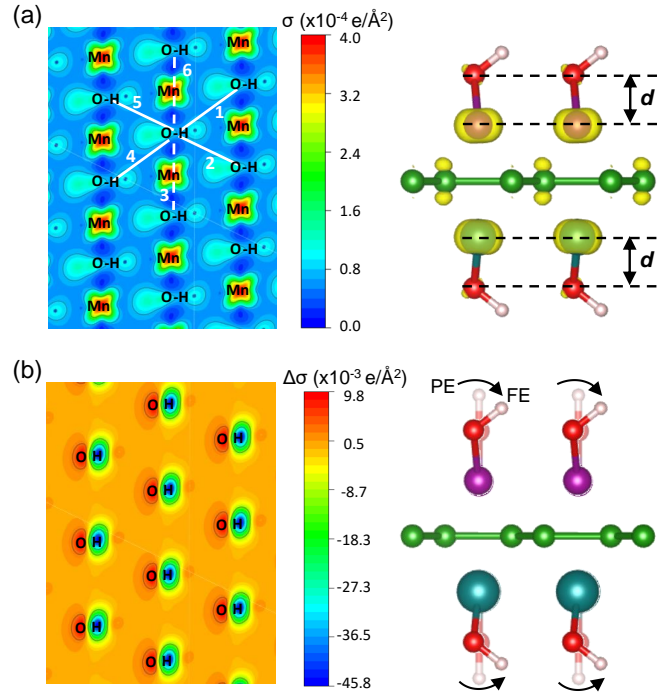


FIG. 3. (a) Partial electron densities contour maps for α -phase MBOH with polarization state of $U\vec{P}_1 + L\vec{P}_1$ taken through atomic plane. The electronic spatial distribution at the Fermi level is shown in the right panel. (b) Charge density difference of between FE state $U\vec{P}_1 + L\vec{P}_1$ and paraelectric (PE) state of α -phase MBOH. The transformation from the PE state to the FE state is illustrated in the right panel.

chains and partially tilted toward to $nh - B$. Due to the orderly arrangement of dipole moments of the $-\text{OH}$ radicals, a macroscopic polarization is established. As the $-\text{OH}$ radicals are distributed on both sides of the $nh - B$, the net polarization comprises polarizations from both the upper $-\text{OH}$ radicals, named as upper polarization ($U\vec{P}$), and the lower ones, named as lower polarization ($L\vec{P}$). Here, we employ a point charge model to evaluate the value of the $U\vec{P}$ and $L\vec{P}$. We do bader charge analysis to get the net charge ΔQ of cations and anions, and measure the distance d between the center of positive charge and negative charge. The values of $U\vec{P}$ and $L\vec{P}$ are then evaluated as $P = \Delta Q \times d = 1.03 \text{ pC}/\text{cm}$.

In spite of using point charge model to evaluate the polarization, it is necessary to prove the existence of the polarization, since the electrostatic forces may be strongly screened by the itinerant electrons in the metallic α -phase MBOH. In Fig. 3(a), we sketched the electron densities of α -phase MBOH around the Fermi level on the atomic planner to have direct view of the charge distribution. We found the conduction charge is mainly spacing around Mn atoms, and rarely spacing around O and H atoms, so we can conclude that the $-\text{OH}$ is a bare ionic radical which is confirmed by the spatial electron distribution exhibited in the right panel of Fig. 3(a). As mentioned

above, the in-plan electrical polarization is coming from the tilting $-\text{OH}$ radicals. From Fig. 3(a), since there is little conduction charges distributed between pair-1, 2, 4 and 5, the screening effect of dipole-dipole interaction in these pairs is small. We should be careful about the screening effect of the pair-3 and 6. It seems that the dipole interactions these two dipole pairs will be screened by the itinerant electrons around Mn atoms. However, the $-\text{OH}$ dipoles and the Mn atoms are separated vertically with distance $d \sim 1.5 \text{ \AA}$, we expect the screening effect actually is limited. This is confirmed by the calculation of the charge difference induced through tilting $-\text{OH}$ radicals from the PE state to the FE state, which is illustrated in the right panel of Fig. 3(b). As shown in left panel of Fig. 3(b), the charge density change $\Delta\sigma$ is plotted. As seen from this plot, we actually did not see a significant redistribution of itinerant electrons around Mn atoms, which affirms conversely the dipole interaction in pair-3 and 6 is slightly screened by the conduction electrons of Mn atoms.

In Fig. 4(a), the *MOM* chains lying on both sides of the $nh - B$ layer align along the same direction, which is marked as direction ‘1’ and is same direction as \vec{a}_2 shown in Fig. 1(a). In the view of stability and physical properties, there are two other equivalent directions, marked as ‘2’ and ‘3’, for *MOM* chains to line up along. For each direction, the $-\text{OH}$ radicals can orient to the right side or the left side of *MOM* chains. We denote the polarization states as $U\vec{P}_n/L\vec{P}_n$ and $U\vec{P}'_n/L\vec{P}'_n$, where $n=1, 2, 3$, indicating the orientation of the *MOM* chains and with or without ‘’ means the $-\text{OH}$ radicals orient to the right or left side of *MOM* chains. Totally, there are six polarization states for $U\vec{P}$ and $L\vec{P}$, as shown in the right panel of Fig. 4(a). The net polarization of the system results from the combination of $U\vec{P}$ and $L\vec{P}$ ($U\vec{P}_n^{(i)} + L\vec{P}_m^{(j)}$, $n, m=1, 2, 3$), leading to thirty-six possible combinations. The combined polarization has four possible values of $0, P, \sqrt{3}P, 2P$ and each non-zero value has six possible corresponding directions. So, there are totally eighteen possible non-zero net polarizations of the system as shown in Fig. 4(b). Each net polarization with magnitude of $P, \sqrt{3}P$ has two possible combinations, while each net polarization with magnitude of $2P$ has one possible combinations. Instead of the term of “possible combination”, in the following we will use the term of “polarization states”. As a result, in α -phase MBOH, there are thirty polarization states possess non-zero net polarization. Based these results, one interesting question is arisen that could the $U\vec{P}/L\vec{P}$ be switched between different states? Since the polarization state is determined by the alignment of *MOM* chains and the orientation of $-\text{OH}$ radicals, we thus categorize the transformation of polarization states into two parts, one is changing the alignment of *MOM* chains, the other is flipping the orientation of $-\text{OH}$ radicals.

For illustrating how to change the alignment of *MOM* chains, here we propose a plausible scenario in Fig. 5(a).

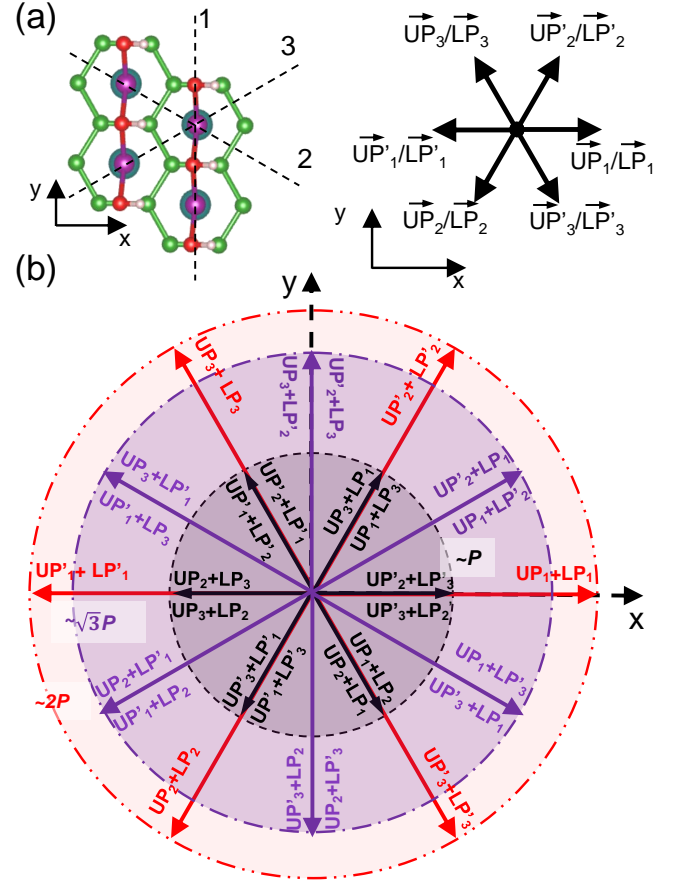


FIG. 4. (a) Three directions along which *MOM* chains could line up, as presented by black dashed lines (left panel), and all possible directions of upper polarization ($U\vec{P}$) and lower polarization ($L\vec{P}$). (b) Eighteen non-zero electrical polarizations of the system, polarization with magnitude of $P, \sqrt{3}P$ and $2P$ are indicated by black solid arrow, purple solid arrow and red solid arrow.

We suppose that a *MOM* chain on the upper side of the $nh - B$ is along direction ‘1’ initially. The $-\text{OH}$ radical connecting Mn_{12} and Mn_{13} firstly swings to the top of B atom, and then move further to connect Mn_{11} and Mn_{13} , forming a *MOM* chain along direction ‘2’, to connect Mn_{11} and Mn_{12} , forming a *MOM* chain along direction ‘3’. The validity of this scenario depends on the initial movement of $-\text{OH}$ towards the top of B, which is supported by the vibration mode of the seventh branch as highlighted by red color in Fig. 5(b). This mode is characterized by the swing of the $-\text{OH}$ radical towards the top of a boron atom. The frequency of this vibration mode at the Γ -point is 117.33 cm^{-1} , which is about 0.56 times of room temperature, meaning that the cost of an external field used to trigger this scenario is acceptable.

Within this model of switching $U\vec{P}/L\vec{P}$, we investigate the energy change ΔE during the process of transforming from $U\vec{P}_1 + L\vec{P}_1$ to $U\vec{P}_2 + L\vec{P}_2$, as shown in Fig. 5(c). In the initial $U\vec{P}_1 + L\vec{P}_1$ state, all *MOM* chains are oriented

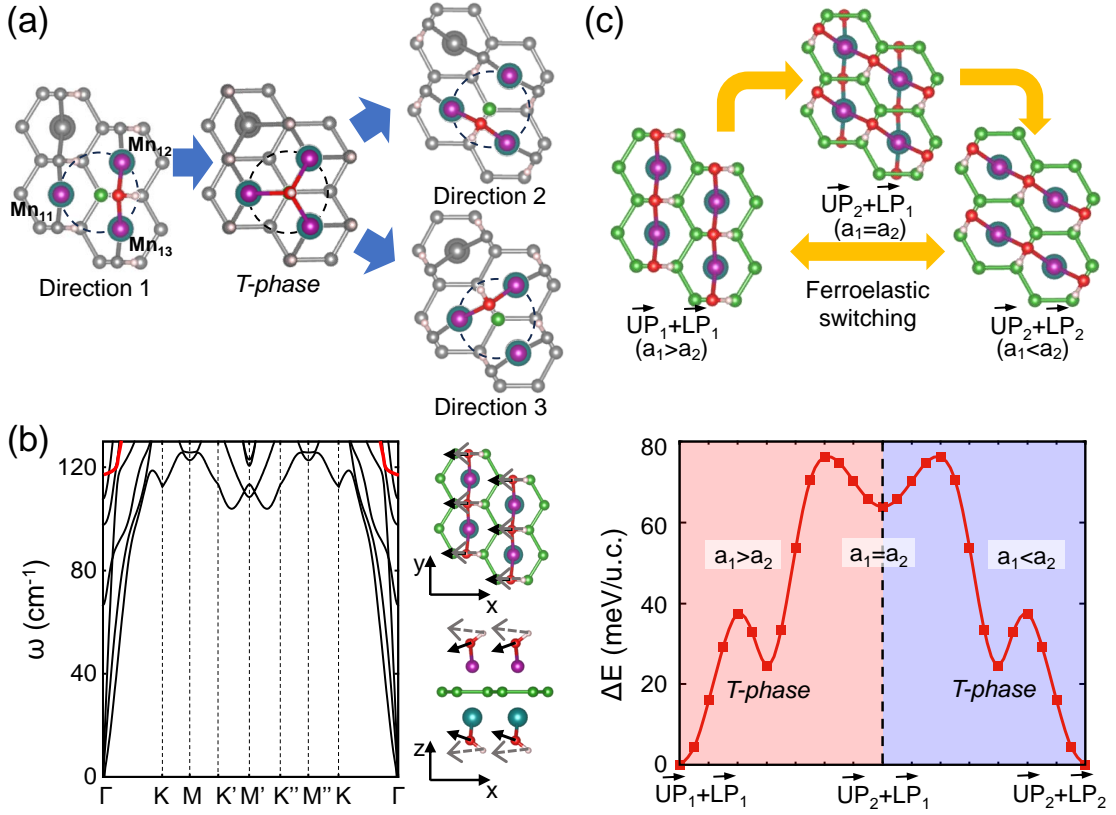


FIG. 5. (a) Schematic mechanism of changing the alignment of the upper *MOM* chains from direction ‘1’ to direction ‘2’ or ‘3’ while fixing the lower *MOM* chains, which undergoes a transition state named as ‘T-phase’. (b) Vibration mode of the special branch of phonon spectra, which is highlighted by red color, indicating the movements of $-\text{OH}$ radicals toward the top of the neighboring B atoms. (c) Illustration of changing polarization state of the system from $\vec{U}\vec{P}_1 + \vec{L}\vec{P}_1$ to $\vec{U}\vec{P}_2 + \vec{L}\vec{P}_2$ and the corresponding DFT-PBE energy difference ΔE encountered during the switching process.

along direction ‘1’, with the lattice constant $a_2 < a_1$. The $\vec{U}\vec{P}_2 + \vec{L}\vec{P}_1$ state is then obtained by twisting the upper *MOM* chains to direction ‘2’, with the lattice constant $a_2 = a_1$. Finally, the lower *MOM* chains change to direction ‘2’, reaching the $\vec{U}\vec{P}_2 + \vec{L}\vec{P}_2$ state, with the lattice constant $a_2 > a_1$. The highest energy barrier is about 75 meV/u.c.. The state of $\vec{U}\vec{P}_1 + \vec{L}\vec{P}_1$ is energetically equally stable as $\vec{U}\vec{P}_2 + \vec{L}\vec{P}_2$, so this polarization switching process is also a ferroelastic process. In other words, the ferroelectricity is coupled with the ferroelasticity and the system exhibits a multiferroic behavior. Besides the stability of the α -phase with upper and lower *MOM* chains aligning along the same direction shown in Fig. 1(c), we also present the stability of the system with upper and lower *MOM* chains aligning along different directions in Fig. 10 of Appendix C.

To flip the orientation of the $-\text{OH}$ radicals with the bond length and bond angle fixed, we vary the dihedral angles ϕ_1/ϕ_2 between Mn-O-Mn plane and y-z plane, and the angle θ_1/θ_2 between the O-H bond and the z-direction as defined in the Fig. 6(a). Taking the transformation from $\vec{U}\vec{P}_1 + \vec{L}\vec{P}_1$ to $\vec{U}\vec{P}'_1 + \vec{L}\vec{P}'_1$ as an example, we study the energy cost during the process in which the net po-

larization is reversed. This process is divided into two steps. The first step is changing $\vec{U}\vec{P}_1$ to $\vec{U}\vec{P}'_1$ through rolling over the $-\text{O}_1\text{H}_1$ radicals at the upper side. The system starts from the initial FE state (FE(+P)) and arrives at an anti-ferroelectric (AFE) state. The second step is changing $\vec{L}\vec{P}_1$ to $\vec{L}\vec{P}'_1$ through rolling over the $-\text{O}_2\text{H}_2$ radicals at the lower side. The system arrives at an FE state with opposite polarization (FE(-P)). The process is illustrated in Fig. 6(b). We calculated the energy change ΔE of the system as a function of θ and ϕ for the two steps of polarization flipping. From the energy map presented in Fig. 6(c), we observe that most of energy cost occurs while changing θ , and the highest energy cost is about $\Delta E = 225 \text{ meV/u.c.}$

C. Spin polarization accompanied with change of polarization state

As shown in Fig. 1(d), the electronic band structure associate with spin-up and spin-down states are degenerate for the system with polarization state of $\vec{U}\vec{P}_1 + \vec{L}\vec{P}_1$. However, the electronic state can be tuned by switching

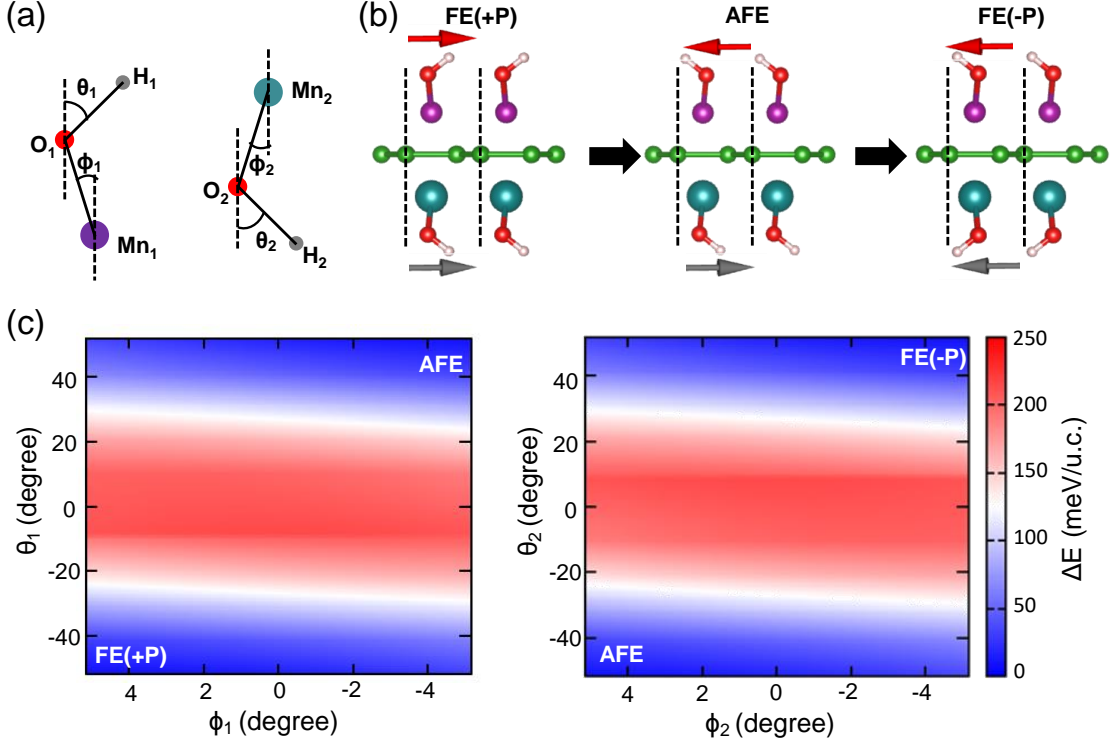


FIG. 6. (a) Dihedral angle ϕ and angle θ used to characterize the position of $-OH$ radicals. (b) Structural change during the polarization flipping path starting from the initial state with polarization $+P$, across the AFE state, and reaching the final state with polarization of $-P$. The polarization directions are indicated by red and grey arrows. (c) Corresponding energy changes ΔE as a function of ϕ and θ during the process of polarization flipping. Subscripts 1 and 2 represent the $-OH$ radicals in the upper layer and lower layer of boron atomic layer, respectively.

polarization states of the system. An illustrative example is presented in Fig. 7(a) for the system featuring the polarization state of $U\vec{P}_2 + L\vec{P}_1$. In this case, the energetic degeneracy of spin-up and spin-down is lifted. More interestingly, the dispersion relation of one spin state appears to replicate the other one, but through a different k -path.

As mentioned above, the difference in the atomic structure between the system with $U\vec{P}_1 + L\vec{P}_1$ and $U\vec{P}_2 + L\vec{P}_1$ is mainly about the alignment of upper MOM chains, as depicted in Fig. 5. Here we present a two-step transformation process in geometry between the two polarization states. As illustrated in Fig. 7(b), we initially rotate the upper MOM chains counterclockwise by 60° to align them with direction ‘2’, resulting in the polarization of $U\vec{P}'_2$. Then, a reflection operation is applied to the upper MOM chains through a mirror plane marked by the blue dashed line in Fig. 7(b), leading to a change in the upper polarization to $U\vec{P}_2$. During the rotating and reflecting operation of upper MOM chains, the atomic sub-unitcell and its corresponding first BZ of the upper MOM chains are transformed in the same way with respect to the fixed cartesian coordinate.

The spin-down and spin-up electronic states originate from the upper and lower MOM chains, respectively,

and they become degenerate when the system is in the state of $U\vec{P}_1 + L\vec{P}_1$. In Fig. 7(b), we manipulate the first BZ referring to the Cartesian coordinates of the upper MOM chains. If we go through Path-2= $\Gamma-K'-M-K-M''-K''-M'-K'-\Gamma$ for the $U\vec{P}'_2$, the energetic dispersion relation of will be the same as the energetic dispersion relation of $U\vec{P}_1$ through Path-1= $\Gamma-K-M-K'-M'-K''-M''-K-\Gamma$. In other words, since the electronic properties are degenerate for $U\vec{P}_1$ and $L\vec{P}_1$, we can assert that the recombination of the band structure of the spin-up states, originating mainly from the lower MOM chains, through Path-2 is a reproduction of the energetic dispersion relation of spin-down states through Path-1 for the system of $U\vec{P}_2 + L\vec{P}_1$. To validate this assertion, we compare the band structure of spin-down states as a function of Path-1 and of spin-up states as a function of Path-2 in Fig. 7(d). The minimal difference observed between them confirms the validity of our analysis. With this clarification, it becomes evident that the electronic properties of spin-up states at $K(K')$, $M'(M'')$ are equivalent to those with spin-down states at $K'(K)$, $M''(M')$, respectively. We present the electronic band structures with spin-up states and spin-down states from Γ point to each individual k point in Fig. 11 of Appendix D. We find that the dispersion relations of spin-up states through $\Gamma-K$,

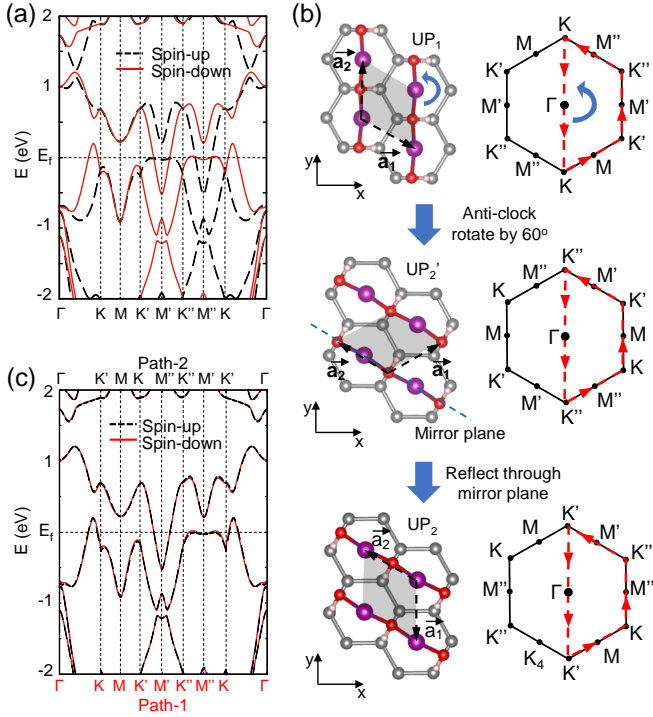


FIG. 7. (a) Spin polarized electronic band structure of α -phase *MBOH* with polarization state of $U\vec{P}_2 + L\vec{P}_1$. (b) Atomic transformation of the system while the $U\vec{P}$ changing from $U\vec{P}_1$ to $U\vec{P}_2$, and accompanied with the transformation of primitive unit-cell and its first Brillouin zone. (c) Reconstruction of band structure with spin-up state along the k-path of $\Gamma-K'-M-K''-M''-K''-\Gamma$ and comparing with band structure with spin-down state along the k-path of $\Gamma-K-M-K'-M'-K''-M''-K'-\Gamma$.

$\Gamma - K'$, $\Gamma - M'$ and $\Gamma - M''$ are identical to that of spin-down states through $\Gamma - K'$, $\Gamma - K$, $\Gamma - M''$ and $\Gamma - M'$.

Considering the splitting of the spin-polarized band structure is decided by electronic spin and the electrons of H atoms are rarely spin-polarized, we can deduce that either H atoms stay at the right side or left side of the *MOM* chains does not impact the band structure splitting. We conducted band structure calculation of the system with $U\vec{P}_2 + L\vec{P}_1$, in which H atoms stay at the opposite side of the upper *MOM* chains in comparison with $U\vec{P}_2 + L\vec{P}_1$. As shown in Fig. 12 of Appendix E, the band structure splitting are the same as that for the system with $U\vec{P}_2 + L\vec{P}_1$.

IV. DISCUSSION

In addition to the physical properties explored above, another noteworthy phenomenon is the formation of an atomic boron layer with a nearly-honeycomb lattice. A presence of the honeycomb lattice of boron is believed to the key factor for the superconductivity in the boron sys-

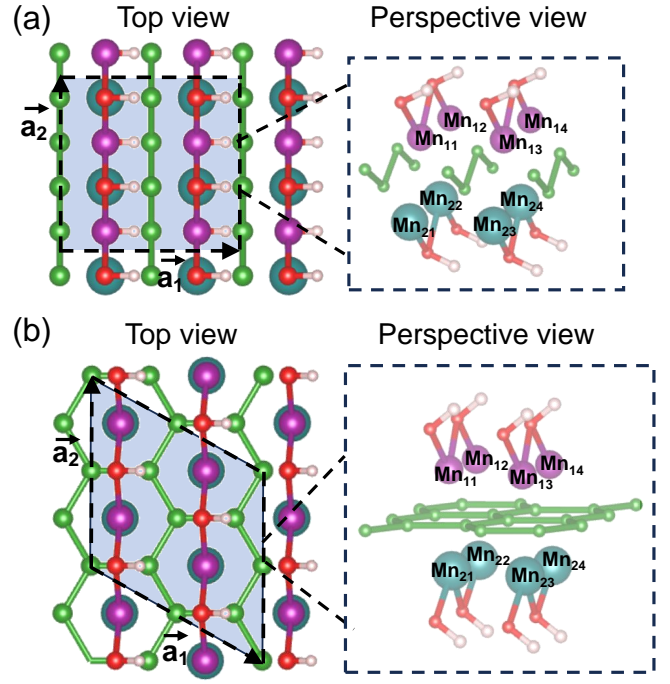


FIG. 8. (a) Precursor structure *MnB* attached with $-OH$ radicals used to searching stable *MBOH* with possible magnetic orders. (b) Precursor structure α -phase *MBOH* with *A-AFM* magnetic order used to searching more stable *MBOH* with other possible magnetic orders. The unit cells used to do structure optimization are highlighted by the transparent blue areas, there are four upper Mn atoms (Mn_{1n}) and four lower Mn atoms (Mn_{2n}) ($n=1, 2, 3, 4$) contained in the unit cell.

tem, such as *MgB₂* [38, 39]. To construct the *MBOH* structure, we start from the initial structure of *Mn₂AlB₂* and attach $-OH$ radicals on the *MnB* framework instead of the Al atoms. The corresponding potential energy change during the conjugate gradient (CG) optimization process is plotted in Fig. 13 of Appendix F. A monotonic decrease of the potential energy is found and almost no energy barrier is observed. This suggests that obtaining the honeycomb lattice of boron is relatively straightforward and no catalysts or other assisting methods are needed in experiments. In comparison to synthesizing the honeycomb lattice of boron through electron doping [40], the use of $-OH$ radical attachment is more direct and applicable on large scale.

We have observed the coexistence and coupling of diverse advanced physical properties in 2D α -phase *MBOH*. To manipulate these properties effectively, it is crucial to control the *MOM* chains and the $-OH$ radicals in the way described in Fig. 6 and Fig. 7. A critical question arises, how can this manipulation be achieved in experiments? Particularly, among these eighteen polarization states, switching from one to the other requests independent manipulation of $-OH$ radicals of the upper or lower layer, which are separated by 7 Å. We propose

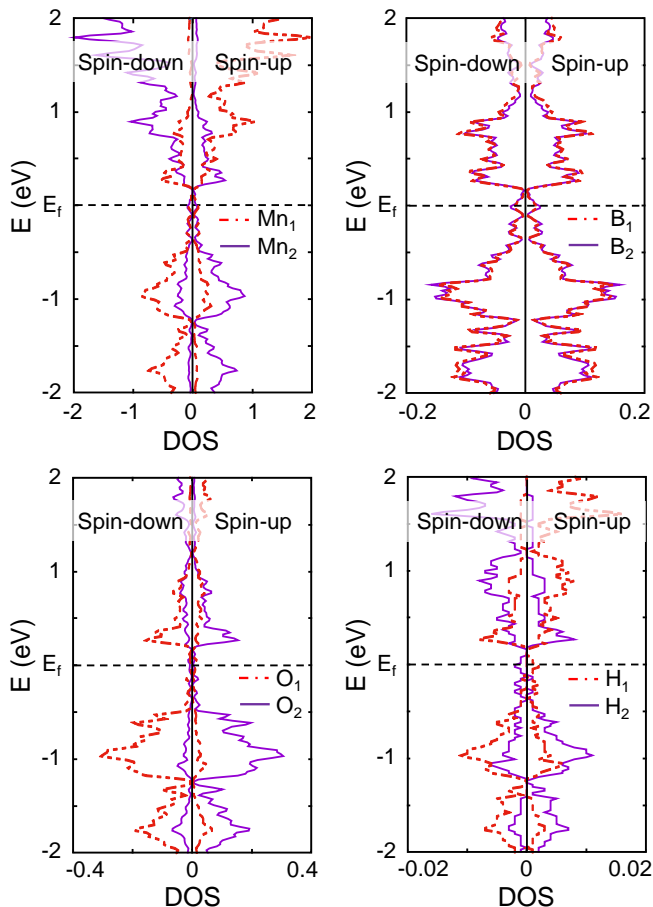


FIG. 9. Spin-polarized projected density of state onto Mn_1 , Mn_2 , B_1 , B_2 , O_1 , O_2 , H_1 , H_2 .

here that scanning tunneling microscopy may be a suitable technique for this purpose [41, 42]. Through controlling the bias voltage, STM can generate an electrical field to change the direction of *MOM* chains in the upper layer while having no effect on the *MOM* chains staying in the lower layer. This approach provides a potential experimental avenue for achieving the desired manipulation.

While all the eighteen polarizations in this study lie in plane, we observe a unique case of the T-phase, as illustrated in Fig. 5(c). This phase, which is about 24.6 meV/u.c. less stable the α -phase, features -OH radicals on one side perpendicular to the plane and that on the other side partially lie in the plane, resulting in a net out-of-plane polarization. This out-of-plane polarization can be flipped by exchanging the orientation modes of -OH radicals of both sides. When combined with these out-of-plane polarizations, the polarization states of the 2D α -phase *MBOH* becomes more attractive.

In the main text, we calculate the electronic band structure of the polarization state of $U\vec{P}_1 + L\vec{P}_1$ and $U\vec{P}_2 + L\vec{P}_1$ to study the effect of the alignment of upper and lower *MOM* chains on the electronic properties,

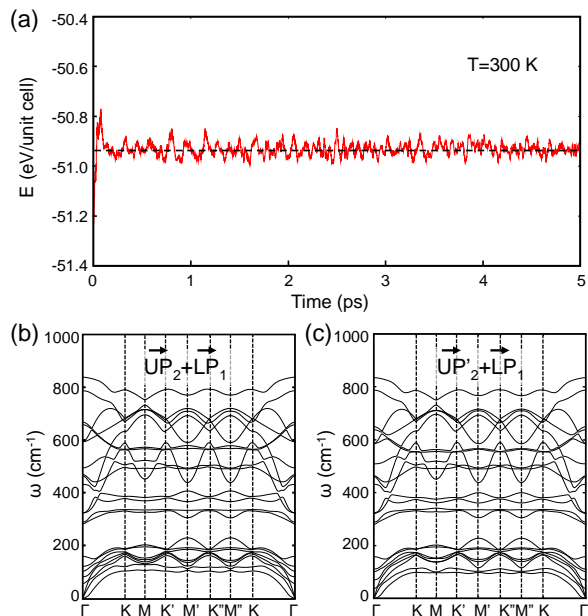


FIG. 10. (a) Change in the potential energy E of polarization state of $U\vec{P}_2 + L\vec{P}_1$ during a 5-ps long canonical MD simulation run at $T=300$ K. (b) DFT-PBE calculated phonon spectra of polarization states of $U\vec{P}_2 + L\vec{P}_1$ and $U\vec{P}'_2 + L\vec{P}_1$.

and we see the spin splitting occurs while the upper and lower *MOM* chains lying in different directions. In addition, we also calculate the band structure of $U\vec{P}'_2 + L\vec{P}_1$ to study the effect of the tilting of -OH radical on the electronic properties, and we see the effect is negligible. Besides these three polarization states, there are other twenty-seven polarization states mentioned in Fig. 4(b), the electronic properties and stabilities of them are similar with these three. In the viewpoint of geometry, the polarization states with a magnitude of $2P$ have a same space group of *Pm*, and these polarization states with the magnitude of P and $\sqrt{3}P$ have a same space group of *C2*. Without changing the relative position of any atom, through appropriate rotation and reflection operation of $U\vec{P}_1 + L\vec{P}_1$, $U\vec{P}_2 + L\vec{P}_1$ or $U\vec{P}'_2 + L\vec{P}_1$, the other twenty-seven polarization states can be achieved. For example, we can rotate the whole structure of $U\vec{P}_1 + L\vec{P}_1$ clockwise by 120 degree to get $U\vec{P}_2 + L\vec{P}_2$; do a reflection to $U\vec{P}_1 + L\vec{P}_2$ through a mirror plane of the boron atoms, we can get $U\vec{P}_2 + L\vec{P}_1$. Since there is no relative space change of any atom during these rigid transformation, we expect the electronic properties and stabilities will be kept after these symmetry operation, and we do not show the band structures of each one here.

V. SUMMARY AND CONCLUSIONS

We study various properties of previously unexplored α -phase of 2D *MBOH*. In contrast to traditional FE

TABLE I. The relative cohesive energy E for the relaxed structure with different magnetic configurations in eV/unit-cell units. E_1 is the cohesive energy for the structure optimized from the precursor MnB attached with $-OH$ radicals with different magnetic configurations. E_2 is the relative cohesive energy for the relaxed structure of the MBOH with different magnetic configurations. The up and down arrows represent the two opposite spin states. E of the most stable structure is set to be 0.

Allotrope	E_1 (eV)	E_2 (eV)	Configuration			
			$Mn_{11}, Mn_{12}, Mn_{13}, Mn_{14}$	$Mn_{21}, Mn_{22}, Mn_{23}, Mn_{24}$		
FM	2.63	1.01	↑	↑	↑	↑
A-AFM	0.00	0.00	↑	↑	↑	↑
F-AFM1	2.78	0.52	↑	↓	↓	↓
F-AFM2	2.23	0.71	↑	↓	↑	↓
F-AFM3	1.63	0.71	↑	↓	↓	↑
A-AFM1	2.53	0.14	↑	↑	↓	↓
A-AFM2	2.23	0.49	↓	↓	↑	↑
A-AFM3	1.53	0.49	↑	↓	↓	↑

materials with only two polarization states, we identify eighteen stable polarization states in this material. We propose a plausible scenario for transformation between these polarization states, which is corroborated by the vibration modes observed in the phonon spectrum. Remarkably, the electric polarization state, which can be tuned through controlling the *MOM* chains, is found coupled with the spin polarization. Furthermore, during the transformation of the electrical polarization, ferroelasticity is observed.

APPENDIX

A. Strategy of exploring allotropes of magnetic MnBOH

Concerning the atomic structure is strongly coupled with the magnetic configuration, start from the precursor MnB shown in Fig. 8(a), we optimize the atomic structure with eight possible magnetic orders. Considering the periodicity of the magnetic order, the atomic structure is optimized using a 2×2 supercell which is four times bigger than the primitive unit cell in Fig. 1(a). There are four upper Mn atoms (labeled as $Mn_{11}, Mn_{12}, Mn_{13}$ and Mn_{14}) and four lower Mn atoms (labeled as $Mn_{21}, Mn_{22}, Mn_{23}$ and Mn_{24}) are contained in the supercell. With respect to the most stable one, the relative cohesive energy E_1 and magnetic configuration of these allotropes

are listed in Table I. We find that the magnetic configuration of the most stable one is the so called A-AFM with intralayer FM coupling and interlayer AFM coupling, and we name this allotrope as α -phase in the main text.

Since we first start from the precursor MnB, and with different magnetic configuration, we optimize the structure and get the most stable α -phase. In case the allotropes with these magnetic configurations are metastable resulted by the chosen precursor of MnB decorating with $-OH$ radicals, we also use the optimized atomic structure of α -phase MnBOH as a precursor but with different magnetic configurations to check the relative stability of the α -phase MnBOH with the A-AFM magnetic order. Same with the above strategy, we use a 2×2 supercell α -phase MnBOH as shown in Fig. 8(b) to do the energy calculation and structure optimization with considering other seven magnetic orders. The relative cohesive energy E_2 is also listed in Table I. We see no matter which precursor we use, the most stable $-OH$ decorating MnB is the α -phase MnBOH.

B. Spin-polarized projected density of state

In order to acquire the magnetic information, we project the density of states onto each element as shown in Fig. 9. For B_1 and B_2 atoms, electrons are equally populated in both channels of spin, which means that the B atoms are not magnetic. For Mn_1, O_1 and H_1 , majority electrons occupy the spin-down channel, while for Mn_2, O_2 and H_2 , majority electrons occupy the spin-up channel. The DFT calculation shows that the magnetic moment of Mn_1, O_1, H_1 is $3.96 \mu_B, 0.06 \mu_B, 0.01 \mu_B$, while that of Mn_2, O_2, H_2 is $-3.96 \mu_B, -0.06 \mu_B, -0.01 \mu_B$, respectively. So, for the system, magnetic moments are mainly coming from the Mn atoms and arranged antiferromagnetically between the upper and lower side of $nh - B$.

C. Thermal stability of polarization state of $U\vec{P}_1 + L\vec{P}_1$, and dynamic stability of polarization states of $U\vec{P}_2 + L\vec{P}_1$ and $U\vec{P}'_2 + L\vec{P}_1$

As mentioned above, the α -phase *MBOH* can have thirty polarization states, some of them have the same polarization magnitude and direction but different atomic structures. Among them, the $U\vec{P}_n + L\vec{P}_n / U\vec{P}'_n + L\vec{P}'_n$ ($n=1, 2, 3$) is the most stable one and the others are less stable by 75 meV/u.c.. In the main manuscript, we show the dynamic stability of $U\vec{P}_n + L\vec{P}_n$, here, we have performed canonical molecular dynamics (MD) simulation of the $U\vec{P}_1 + L\vec{P}_1$ at room temperature ($T=300$ K) for a time period of 10 ps. As seen in Figure 10(a), the potential energy fluctuates around a constant value, indicating that the structure are dynamically stable at room

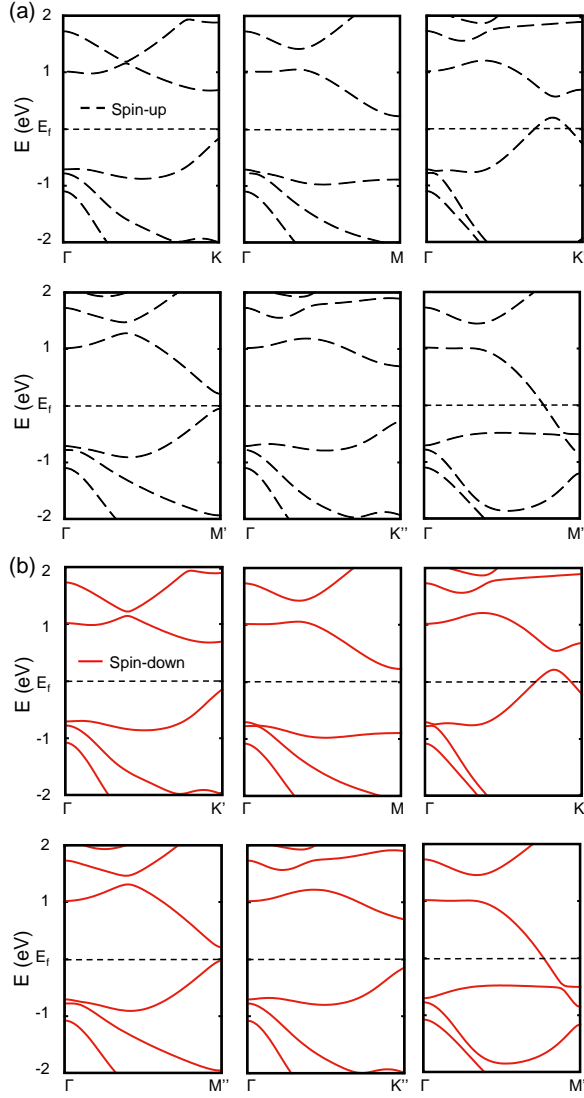


FIG. 11. Electronic energy-momentum dispersion relation from Γ to each k point of α -phase *MBOH* with (a) spin-up state, (b) spin-down state.

temperature. As shown in Figure 10(b), we have also calculated phonon spectra of $U\vec{P}_2 + L\vec{P}_1$ and $U\vec{P}'_2 + L\vec{P}_1$ as representative of these less stable ones. All spectra are free of imaginary frequencies, meaning that except the most stable ones of $U\vec{P}_n + L\vec{P}_n/U\vec{P}'_n + L\vec{P}'_n$, the other energetic less stable polarization states are also dynamically stable.

D. Decomposition of Electronic Band Structure of α -phase *MBOH* with Polarization State $U\vec{P}_2 + L\vec{P}_1$

As we discussed, the splitting of band structure for α -phase *MBOH* with polarization status of $U\vec{P}_2 + L\vec{P}_1$ is coming from the transformation between corresponding reciprocal lattices of the sub atomic structures with spin-

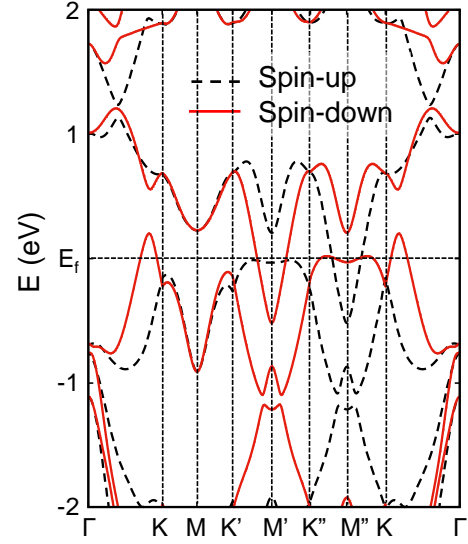


FIG. 12. Spin polarized electronic band structure of α -phase *MBOH* with electrical polarization status of $U\vec{P}'_2 + L\vec{P}_1$.

up and spin-down states. The electronic properties for the sub atomic structure with spin-up at momentum of K, K', M', M'' are equivalent with that for the sub atomic structure with spin-down at momentum of K', K, M'', M' . We show the electronic energy-momentum dispersion relations of spin-up and spin-down states from Γ to each k point in Figures 11. We see the dispersion relation of spin-up state in the path of Γ - K, Γ - K', Γ - M', Γ - M'' in Figures 11(a) are the same with dispersion relation of spin-down state in the path of Γ - K', Γ - K, Γ - M'', Γ - M' in Figures 11(b) correspondingly, which proves the validity of our conclusion.

E. Electronic Band Structure of α -phase *MBOH* with Polarization of $U\vec{P}'_2 + L\vec{P}_1$

We calculate the electronic band structure of α -phase *MBOH* with polarization status of $U\vec{P}'_2 + L\vec{P}_1$ as shown in Figure 12. The difference in atomic structure of α -phase *MBOH* between the polarization status of $U\vec{P}'_2 + L\vec{P}_1$ and $U\vec{P}_2 + L\vec{P}_1$ is the orientation of $-OH$ radicals, but the spin polarized band structure of the two polarization status are identical. In other words, as we mention in the main manuscript, whether the H atoms are staying at the right side or left side of the *MOM* chain has no effect on the band structure.

F. Formation of α -phase *MBOH*

In main manuscript, we mentioned that a 2D boron with nearly-honeycomb lattice is formed in α -phase *MBOH*, which is meaningful for studying the superconductivity in boron system. For real experiment, we

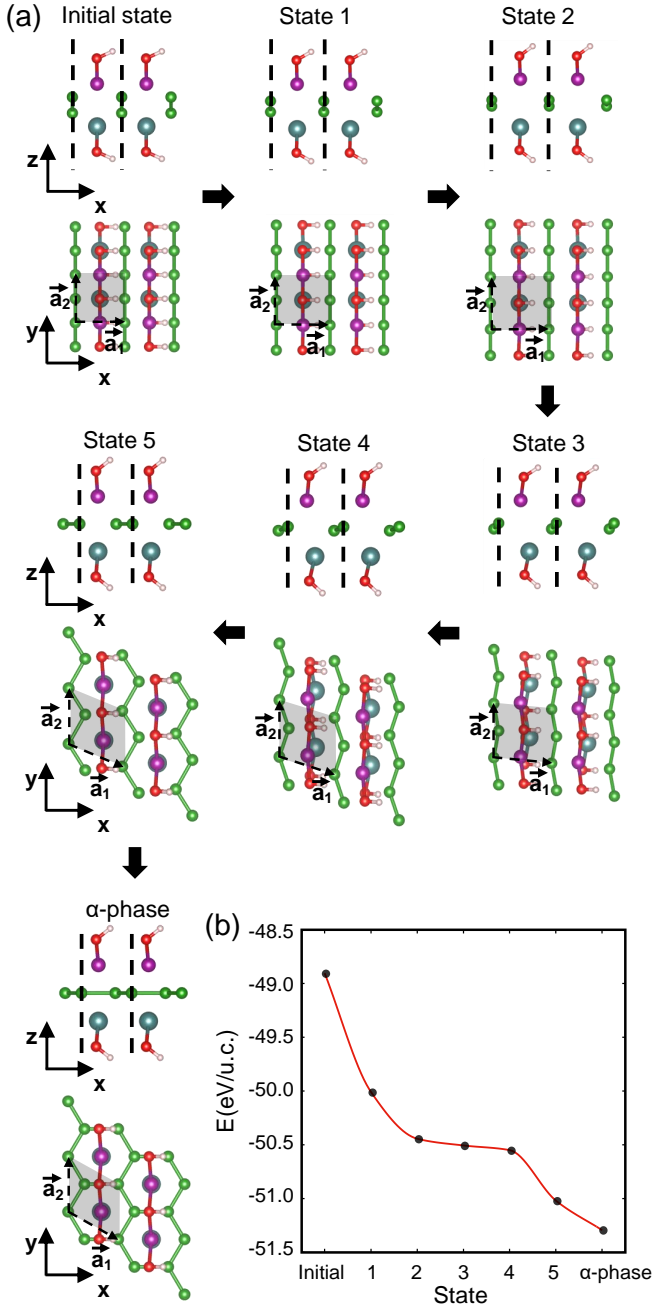


FIG. 13. (a) Schematic illustration of the atomic structure evolution from the structure with $-OH$ radicals attached on the precursor MnB to the stable α -phase $MBOH$ during the CG optimization. (b) Potential energy E as a function of several picked states of $MBOH$ presented in (a) during the structure optimization.

need to analysis the feasibility of synthesising such material. In our calculation, we use the CG method to do the structure optimization. This method can provide a figure of merit about the evolution from the initial state to the final optimized state. We present several snapshots of the system during the optimization process in Figure 13(a) to illustrate the formation of the α -phase $MBOH$ from the precursor MnB with $-OH$ radicals attached. Corresponding with these states, the potential energy E of the system is shown in Figure 13(b). We see that from the initial state to the α -phase, E decreases monotonically, which indicates α -phase is relatively easy to be synthesised in experiment using $-OH$ radicals to decorate the MnB.

ACKNOWLEDGMENTS

This study is supported by the Natural Science Foundation of the Jiangsu Province (Grant No. BK20210198), the National Natural Science Foundation of China (Grant Nos. 62274028, 12204095 and 12104090), the High Level Personnel Project of Jiangsu Province Grant No. JSSCBS20220120, ‘Zhishan’ Scholars Program of Southeast University (Grant Nos. 2242023R10006 and 2242021R40004), open research fund of Key Laboratory of Quantum Materials and Devices (Southeast University) of Ministry of Education, and the Fundamental Research Funds for the Central Universities (Southeast University).

Pingwei Liu and Dan Liu contributed equally to this work.

[1] K. S. Novoselov, A. K. Geim, S. V. Morozov, D. Jiang, Y. Zhang, S. V. Dubonos, I. V. Grigorieva, and A. A. Firsov, Electric field effect in atomically thin carbon films, *Science* **306**, 666 (2004).

[2] S. Barraza-Lopez, B. M. Fregoso, J. W. Villanova, S. S. P. Parkin, and K. Chang, Colloquium: Physical properties of group-iv monochalcogenide monolayers, *Rev. Mod. Phys.* **93**, 011001 (2021).

- [3] W. Ding, J. Zhu, Z. Wang, Y. Gao, D. Xiao, Y. Gu, Z. Zhang, and W. Zhu, Prediction of intrinsic two-dimensional ferroelectrics in $\text{in}2\text{se}3$ and other $\text{iii}2\text{-vi}3$ van der waals materials, *Nat. Commun.* **8**, 14956 (2017).
- [4] A. Belianinov, Q. He, A. Dziazgys, P. Maksymovych, E. Eliseev, A. Borisevich, A. Morozovska, J. Banys, Y. Vysochanskii, and S. V. Kalinin, CuInP_2S_6 room temperature layered ferroelectric, *Nano Lett.* **15**, 3808 (2015).
- [5] Z. Fei, W. Zhao, T. A. Palomaki, B. Sun, M. K. Miller, Z. Zhao, J. Yan, X. Xu, and D. H. Cobden, Ferroelectric switching of a two-dimensional metal, *Nature* **560**, 336 (2018).
- [6] D. Liu, L. Han, R. Wei, S. Song, J. Guan, S. Dong, and D. Tománek, Unusual electric polarization behavior in elemental quasi-two-dimensional allotropes of selenium, *Phys. Rev. Materials* **6**, 103403 (2022).
- [7] C. Cui, F. Xue, W. Hu, and L. Li, Two-dimensional materials with piezoelectric and ferroelectric functionalities, *npj 2D Mater. Appl.* **2**, 1 (2018).
- [8] Z. Guan, H. Hu, X. Shen, P. Xiang, N. Zhong, J. Chu, and C. Duan, Recent progress in two-dimensional ferroelectric materials, *Adv. Electron. Mater.* **6**, 1900818 (2020).
- [9] L. Qi, S. Ruan, and Y. Zeng, Review on recent developments in 2d ferroelectrics: Theories and applications, *Adv. Mater.* **33**, 2005098 (2021).
- [10] Z. Fei, B. Huang, P. Malinowski, W. Wang, T. Song, J. Sanchez, W. Yao, D. Xiao, X. Zhu, A. F. May, W. Wu, D. H. Cobden, J. Chu, and X. Xu, Two-dimensional itinerant ferromagnetism in atomically thin Fe_3GeTe_2 , *Nat. Mater.* **17**, 778 (2018).
- [11] B. Huang, G. Clark, D. R. Klein, D. MacNeill, E. Navarro-Moratalla, K. L. Seyler, N. Wilson, M. A. McGuire, D. H. Cobden, D. Xiao, W. Yao, P. Jarillo-Herrero, and X. Xu, Electrical control of 2d magnetism in bilayer CrI_3 , *Nat. Nanotechnol.* **13**, 544 (2018).
- [12] B. Huang, G. Clark, E. Navarro-Moratalla, D. R. Klein, R. Cheng, K. L. Seyler, D. Zhong, E. Schmidgall, M. A. McGuire, D. H. Cobden, W. Yao, D. Xiao, P. Jarillo-Herrero, and X. Xu, Layer-dependent ferromagnetism in a van der waals crystal down to the monolayer limit, *Nature* **546**, 270 (2017).
- [13] M. Gibertini, M. Koperski, A. F. Morpurgo, and K. S. Novoselov, Magnetic 2d materials and heterostructures, *Nat. Nanotechnol.* **14**, 408 (2019).
- [14] M. Blei, J. L. Lado, Q. Song, D. Dey, O. Erten, V. Pardo, R. Comin, S. Tongay, and A. S. Botana, Synthesis, engineering, and theory of 2d van der waals magnets, *Appl. Phys. Rev.* **8**, 021301 (2021).
- [15] H. Wang, X. Li, Y. Wen, R. Cheng, L. Yin, C. Liu, Z. Li, and J. He, Two-dimensional ferromagnetic materials: From materials to devices, *Appl. Phys. Lett.* **121**, 220501 (2022).
- [16] M. Yankowitz, S. Chen, H. Polshyn, Y. Zhang, K. Watanabe, T. Taniguchi, D. Graf, A. F. Young, and C. R. Dean, Tuning superconductivity in twisted bilayer graphene, *Science* **363**, 1059 (2019).
- [17] C. Xu, L. Wang, Z. Liu, L. Chen, J. Guo, N. Kang, X. Ma, H. Cheng, and W. Ren, Large-area high-quality 2d ultrathin Mo_2C superconducting crystals, *Nat. Mater.* **14**, 1135 (2015).
- [18] A. W. Tsien, B. Hunt, Y. D. Kim, Z. J. Yuan, S. Jia, R. J. Cava, J. Hone, P. Kim, C. R. Dean, and A. N. Pasupathy, Nature of the quantum metal in a two-dimensional crystalline superconductor, *Nat. Phys.* **12**, 208 (2016).
- [19] Y. Saito, T. Nojima, and Y. Iwasa, Highly crystalline 2d superconductors, *Nat. Rev. Mater.* **2**, 16094 (2017).
- [20] D. Qiu, C. Gong, S. Wang, M. Zhang, C. Yang, X. Wang, and J. Xiong, Recent advances in 2d superconductors, *Adv. Mater.* **33**, 2006124 (2021).
- [21] K. S. Novoselov, A. Mishchenko, A. Carvalho, and A. H. Castro Neto, 2d materials and van der waals heterostructures, *Science* **353**, 9439 (2016).
- [22] P. V. Pham, S. C. Bodepudi, K. Shehzad, Y. Liu, Y. Xu, B. Yu, and X. Duan, 2d heterostructures for ubiquitous electronics and optoelectronics: Principles, opportunities, and challenges, *Chem. Rev.* **122**, 6514 (2022).
- [23] P. Solis-Fernandez, M. Bissett, and H. Ago, Synthesis, structure and applications of graphene-based 2d heterostructures, *Chem. Soc. Rev.* **46**, 4572 (2017).
- [24] E. Pomerantseva and Y. Gogotsi, Two-dimensional heterostructures for energy storage, *Nat. Energy* **2**, 17089 (2017).
- [25] Y. Liu, S. Zhang, J. He, Z. M. Wang, and Z. Liu, Recent progress in the fabrication, properties, and devices of heterostructures based on 2d materials, *Nano-Micro Lett.* **11**, 13 (2019).
- [26] Q. Song, C. A. Occhialini, E. Ergecen, B. Ilyas, D. Amoroso, P. Barone, J. Kapteghian, K. Watanabe, T. Taniguchi, A. S. Botana, S. Picozzi, N. Gedik, and R. Comin, Evidence for a single-layer van der waals multiferroic, *Nature* **602**, 601 (2022).
- [27] C. Liu, W. Ren, and S. Picozzi, Spin-chirality-driven multiferroicity in van der waals monolayers, *Phys. Rev. Lett.* **132**, 086802 (2024).
- [28] J. Ji, G. Yu, C. Xu, and H. J. Xiang, General theory for bilayer stacking ferroelectricity, *Phys. Rev. Lett.* **130**, 146801 (2023).
- [29] S. P. Poudel, J. M. Marmolejo-Tejada, J. E. Roll, M. A. Mosquera, and S. Barraza-Lopez, Creating a three-dimensional intrinsic electric dipole on rotated CrI_3 bilayers, *Phys. Rev. B* **107**, 195128 (2023).
- [30] G. Kresse and J. Furthmüller, Efficient iterative schemes for *ab initio* total-energy calculations using a plane-wave basis set, *Phys. Rev. B* **54**, 11169 (1996).
- [31] G. Kresse and D. Joubert, From ultrasoft pseudopotentials to the projector augmented-wave method, *Phys. Rev. B* **59**, 1758 (1999).
- [32] J. P. Perdew, K. Burke, and M. Ernzerhof, Generalized gradient approximation made simple, *Phys. Rev. Lett.* **77**, 3865 (1996).
- [33] A. I. Liechtenstein, V. I. Anisimov, and J. Zaanen, Density-functional theory and strong interactions: Orbital ordering in mott-hubbard insulators, *Phys. Rev. B* **52**, R5467 (1995).
- [34] H. J. Monkhorst and J. D. Pack, Special points for Brillouin-zone integrations, *Phys. Rev. B* **13**, 5188 (1976).
- [35] M. R. Hestenes and E. Stiefel, Methods of conjugate gradients for solving linear systems, *J. Res. Natl. Bur. Stand.* **49**, 409 (1952).
- [36] A. Togo and I. Tanaka, First principles phonon calculations in materials science, *Scr. Mater.* **108**, 1 (2015).
- [37] Y. Wang, W. Xu, D. Yang, Y. Zhang, Y. Xu, Z. Cheng, X. Mi, Y. Wu, Y. Liu, Y. Hao, and G. Han, Above-room-temperature strong ferromagnetism in 2d mnb nanosheet, *ACS nano* **17**, 24320 (2023).

- [38] W. Kang, H. Kim, E. Choi, C. Jung, and S. Lee, MgB₂ superconducting thin films with a transition temperature of 39 kelvin, *Science* **292**, 1521 (2001).
- [39] S. Souma, Y. Machida, T. Sato, T. Takahashi, H. Matsui, S. Wang, H. Ding, A. Kaminski, J. Campuzano, S. Sasaki, and K. Kadowaki, The origin of multiple superconducting gaps in MgB₂, *Nature* **423**, 65 (2003).
- [40] D. Liu and D. Tománek, Effect of net charge on the relative stability of 2d boron allotropes, *Nano Lett.* **19**, 1359 (2019).
- [41] M. Alemani, M. V. Peters, S. Hecht, K.-H. Rieder, F. Moresco, and L. Grill, Electric field-induced isomerization of azobenzene by stm, *J. Am. Chem. Soc.* **128**, 14446 (2006).
- [42] J. Zhang, J. Zhong, J. Lin, W. Hu, K. Wu, G. Xu, A. T. S. Wee, and W. Chen, Towards single molecule switches, *Chem. Soc. Rev.* **44**, 2998 (2015).